

A Mixture-Fraction–Based Hybrid Binomial Langevin–Multiple Mapping Conditioning Model

Andrew P. Wandel^{a,b}, R. Peter Lindstedt^c

^a*University of Southern Queensland,
Computational Engineering and Science Research Centre,
School of Mechanical and Electrical Engineering,
Toowoomba, 4350, Australia*

^b*Corresponding author. Fax: +61 7 4631 2526; E-mail: andrew.wandel@usq.edu.au*

^c*Department of Mechanical Engineering,
Imperial College London,
London, SW7 2BX, UK*

Abstract

Generalized Multiple Mapping Conditioning (MMC) allows for the use of any physical quantity to represent the required reference variable provided that it delivers the desired behavior. The binomial Langevin model (BLM) has been shown to predict higher statistical moments with good accuracy. However, joint–scalar modeling for many scalars becomes problematic because scalar bounds must be specified as conditional on other scalars to preserve elemental balances. The resulting volumes in state space become exceptionally complex for realistic problem sizes. In the current work, this central difficulty is avoided by using only velocity and mixture fraction statistics from the BLM with the latter used as the MMC reference variable. The principal advantage of this method is that the implementation of the binomial Langevin mixture fraction is relatively straightforward and provides a direct physical link to MMC. The MMC model is closed using an augmented modified Curl’s model where the selection of particle pairs for (turbulent)

mixing ensures proximity in reference space and a corresponding closeness in physical space. The method is evaluated for a lifted methane jet flame undergoing auto-ignition in a vitiated coflow. Most of the major features of the flow are well reproduced and found to generally outperform other modeling approaches, including Large Eddy Simulations using simplified treatments of turbulence–chemistry interactions such as unsteady flamelet/progress variable descriptions.

Keywords: Turbulent combustion, Multiple Mapping Conditioning, MMC, Langevin models, Lifted flame

Colloquium: 5. Turbulent Flames

Word count (= 6193) calculation.

Item	Size	Units	Multiplier	Words
Text	6.5	pages	900	5850
Last bit	156	mm	2.2	343
Total				6193

There is no need for color reproduction: grayscale is satisfactory.

There is Supplemental Material (13 figures).

1. Introduction

The desire to combine improved combustion efficiency with lower emissions has led to an increased interest in combustion systems that operate near stability limits. Finite-rate chemistry effects (such as extinction/reignition) become important under such conditions and the formulation of calculation methods capable of reproducing such phenomena has received substantial interest [1, 2, 3, 4]. Time-scales covering several orders of magnitude become important [5] with turbulence typically interacting strongly with chemical kinetics. Simple models cannot capture such phenomena and transported probability density function (PDF) based models are typically required [6, 7]. Predictions are more sensitive to various model components—including the closure for molecular mixing [8]—in such situations.

The hybrid binomial Langevin–Multiple Mapping Conditioning (MMC) model [9, 10] aims to combine some of the benefits of the binomial Langevin model (BLM) [11], such as predictions of higher statistical moments, with the benefits of the MMC approach [12], while overcoming at least some of the deficiencies associated with each individual model component. Previously, the hybrid model utilized a velocity component for mapping the MMC mixture fraction. The current work replaces the velocity with a mixture fraction to provide a more physical basis for general flames.

One of the difficulties with BLM is joint–scalar modeling because the bounds for all scalars must be specified as conditional on all other scalars to conserve elemental balances. A formulation of the joint velocity–scalar PDF that includes the joint statistics of a mixture fraction and a reaction progress variable has been developed [13]. The formulation provides detailed statistics

26 of velocity–scalar interactions, predicting higher moments with encouraging
27 accuracy. The current hybrid model seeks to retain this ability while averting
28 the central difficulty of evolving (variable) scalar bounds.

29 In the MMC framework, a mathematical reference space is utilized that
30 has sufficient dimensions in scalar space to describe the manifold on which
31 compositions may lie [14]. This is founded on the principles of ordinary
32 and doubly-conditioned Conditional Moment Closures (CMC) [15] applied
33 in previous studies [16, 17, 18]. The probabilistic approach [19] (similar to
34 second-order CMC) provides an alternative [20], has been implemented in a
35 variety of ways [21, 22, 23], and forms the basis for the MMC component of
36 the current hybrid model.

37 Surrogate reference variables have been developed for MMC to avoid dif-
38 ficulties in specifying model coefficients: some quantity (preferably already
39 solved as part of the calculation procedure) is used as the reference variable.
40 This is fundamental to the application of generalized MMC [24, 25, 26]. The
41 transformation of such a quantity into a reference variable has been utilized in
42 sparse Lagrangian Large Eddy Simulations (LES) by using the LES-resolved
43 filtered mixture fraction field [24, 27, 28]. In the current hybrid approach, the
44 mixture fraction obtained from BLM is used as the reference variable. The
45 scalar mixing in the MMC component of the hybrid model is then controlled
46 by specifying the fraction of particles which are to be mixed. The model
47 is evaluated by simulating a fuel jet undergoing auto-ignition in a vitiated
48 coflow [29].

49 **2. Theory**

50 *2.1. Binomial Langevin model*

51 Hulek and Lindstedt [13] developed a generalized form of BLM [11] for
 52 the joint-PDF of velocity and multiple scalars. The velocity transport model
 53 (including the turbulent dissipation ε , the return-to-isotropy of the Reynolds
 54 stresses and the dispersion in velocity space) for a stochastic particle p is:

$$du_i^{*p} = \frac{1}{\tau_u} (\alpha_1 \delta_{ij} + \alpha_2 \beta_{ij}) (u_j^{*p} - \langle u_j \rangle) dt + (C_0 \langle \varepsilon \rangle)^{1/2} dw_i \quad (1)$$

55 where superscript ‘*’ represents a stochastic trajectory, k is the turbulent
 56 kinetic energy, the velocity time-scale is $\tau_u = \langle k \rangle / \langle \varepsilon \rangle$, dw_i is an isotropic
 57 Wiener process and the Reynolds stress anisotropy tensor is

$$\beta_{ij} = \frac{\langle u'_i u'_j \rangle}{\langle u'_k u'_k \rangle} - \frac{\delta_{ij}}{3}. \quad (2)$$

58 The modeling coefficients are $C_0 = 2.1$, $\alpha_2 = 3.7$ and $\alpha_1 = -(\frac{1}{2} + \frac{3}{4}C_0) -$
 59 $\alpha_2 \beta_{ii}^2$. The modeled stochastic differential equation for any scalar η is

$$d\eta^{*p} = \frac{G_\eta}{2\tau_\eta} (\eta^{*p} - \langle \eta \rangle) dt + (B_\eta \langle \varepsilon_\eta \rangle)^{1/2} dw_{\text{bin}} \quad (3)$$

60 where the drift (G_η) and diffusion (B_η) coefficients are defined elsewhere [11,
 61 13], dw_{bin} is a binomial Wiener process [11] and the mean scalar dissipation
 62 is modeled as $\langle \varepsilon_\eta \rangle \equiv \langle \eta'^2 \rangle / \tau_\eta$, with the scalar timescale modeled using the
 63 timescale ratio C_ϕ :

$$\tau_\eta = \tau_u / C_\phi. \quad (4)$$

64 Many of the physical processes that occur are simulated well by the
 65 model [13]. However, the presence of conditional scalar limits in G_η and

66 B_η for reacting scalars cause difficulties due to evolving scalar bounds. This
 67 issue has been addressed for a two-scalar formulation by ensuring transport
 68 along a scalar boundary for limiting cases [13]. Generally, a much larger
 69 number of scalars (e.g. 48 species in the current case) must be considered,
 70 resulting in very complex volumes in composition space. However, if the im-
 71 plementation is restricted to the mixture fraction alone (where the bounds
 72 are simple), then no difficulties arise.

73 *2.2. MMC model*

74 The current work utilizes Generalized MMC [26], so does not solve the
 75 standard transport equation for the reference variable (ξ^{*p}) [12], because the
 76 mixture fraction solved by the binomial Langevin model is defined to be the
 77 reference variable:

$$\xi^{*p} = \eta^{*p} . \tag{5}$$

78 Instead, the transport of the reference variable is solved by Eq. (3). The same
 79 particle contains information from both the BLM and MMC, so η directly
 80 maps to the MMC mixture fraction Z . The major benefits of this approach
 81 are that the reference variable does not merely map, but actually models the
 82 behavior of the mixture fraction; and the inhomogeneous drift term, which
 83 is challenging to model, does not need to be determined.

84 Equation (5) is the principal difference with the previous hybrid binomial
 85 Langevin–MMC model [9, 10]; previously the velocity from Eq. (1) was used
 86 to define ξ in Eq. (5). Because η was used in the earlier work to control the
 87 amount of mixing, another model for the mixing needs to be implemented,
 88 which will be discussed later.

89 In the MMC framework, n_s reactive scalars are solved with $n_s - 1$ species
 90 mass fractions (Y_I) combined with the specific enthalpy h . The stochastic
 91 form of the transport equations is [12]:

$$dZ^{*p} = Sdt \quad (6)$$

$$dY_I^{*p} = (S + W_I)dt \quad (7)$$

$$d\mathbf{x}^{*p} = \mathbf{U}dt. \quad (8)$$

92 Here, S is the mixing model, W_I the chemical source term, dw_l a Wiener
 93 process and $\mathbf{U} \equiv \langle \mathbf{v} | \boldsymbol{\xi} \rangle$ the conditional velocity, with \mathbf{v} the physical velocity.
 94 To ensure compatibility with the joint-PDF of mixture fraction and velocity
 95 for BLM, the BLM velocity obtained from Eq. (1) is used in Eq. (8) for the
 96 current hybrid model:

$$\mathbf{U} = \mathbf{u}. \quad (9)$$

97 The conventional model for the diffusion coefficient B was used

$$B = \frac{\langle \varepsilon_\eta \rangle}{2} \left\langle \left(\frac{\partial Z}{\partial \xi} \right)^2 \right\rangle^{-1}, \quad (10)$$

98 with the derivative obtained by subdividing the reference space and perform-
 99 ing least-squares curve fits in each section [30].

100 The Modified Curl's (MC) model [31, 32] was applied for the mixing term
 101 (S). What distinguishes MMC from MC is that pairs of particles are not ran-
 102 domly paired, which could cause interaction across a diffusion layer (which
 103 would only happen in extremely high turbulence). Instead pairs of particles
 104 are selected to be close in reference space, modeling the behavior that par-
 105 ticles are physically close together (at a subgrid scale) because the mapping
 106 process requires the reference variable to change across a diffusion layer in

107 a similar way to the mixture fraction. Particles are considered available for
 108 pairing according to [10, 30]

$$|\Delta\xi^{*pq}| \leq (2B\Delta t)^{1/2} \quad (11)$$

109 where $\Delta\xi^{*pq} = \xi^{*q} - \xi^{*p}$. This mimics the effect of the diffusive term of a
 110 stochastic differential equation [i.e. the last term of Eq. (1) or Eq. (3)], where
 111 the average distance particles diffuse is $(2B\Delta t)^{1/2}$ and the particles interact
 112 at the new location. To reduce the chances of Eq. (11) being violated, p
 113 is selected so that $|\xi^{*p}|$ is in descending order. If no q can be found to
 114 satisfy Eq. (11), then q is selected to minimize $|\Delta\xi^{*pq}|$ and any violation will
 115 occur for outliers, which are in the low-probability region. In common with
 116 all other PDF-based approaches where particles mix by sharing information
 117 with a small number of particles (usually one other), if Δt is too small or the
 118 number of particles is insufficient (i.e. if $n_p\Delta t \rightarrow 0$, where n_p is the number
 119 of particles in a physical cell), then the model fails ($\langle Z'^2 \rangle$ does not decay in
 120 the mixing substep).

121 Particles are paired with a nearby particle, not the neighboring parti-
 122 cle. The reason for this is that smaller values of $n_p\Delta t$ are possible without
 123 changing the result. Those MMC methods which pair neighboring particles,
 124 e.g. [33, 21], rely on sufficiently-high values of $n_p\Delta t$ to reorder the particles
 125 so particles do not uniquely pair with the same particle repeatedly. Such
 126 behavior is also observed in the stranding behavior of EMST if it is imple-
 127 mented without the aging function, which causes many of the particles to be
 128 unavailable for interactions. Arguably, the low $n_p\Delta t$ limit of MMC behaves
 129 worse than EMST in terms of stranding: MMC is restricted to isolated pairs
 130 of particles, whereas in EMST interactions can occur between multiple par-

131 ticles. The method used here and in related work [9, 10, 20, 30] guarantees
132 dissipation in the mixing process for smaller values of $n_p\Delta t$ than methods
133 that pair neighboring particles. Because the distance between particles in
134 reference space is consequentially greater for individual particles than if they
135 were neighboring, the amount of dissipation per mixing interaction and the
136 number of paired particles must also be different.

137 To close the model for S , the MC model [31, 32] was used. The process of
138 choosing the degree of mixing differs from the previous model because η is not
139 available for controlling this process. For those particles selected for mixing,
140 the amount of mixing was 50% [30] of that specified in the original Curl's
141 model. The number of particles selected for mixing remains an unclosed
142 parameter. In the current work, 6% of particles at any physical location
143 were mixed per time step; on average, this amounted to 24 particles. It is
144 likely that this value of 6% is not general and future work will focus on a
145 general approach to selecting the number of particles to mix.

146 The method of mixing follows the same procedure as standard MC.
147 Firstly, the method for choosing pairs must be decided. In MC, particles are
148 randomly chosen from the available set of particles (normally those within a
149 computational cell, so the particles are moderately close in physical space).
150 In the current method, the pair for a particle is chosen at random from
151 the subset of particles within the computational cell that are also close in
152 reference space. Secondly, the distribution of the mixing amount must be
153 chosen. A uniform distribution is common for MC (the amount of mixing
154 is a uniformly-distributed random variable between no mixing and complete
155 mixing). The current method specifies a single value that provides the same

156 mean amount of mixing [30]; modifying this to a random value affects the
157 conditional means [30]. Finally, the fraction of particles to be mixed must
158 be determined. In MC, this is governed by the distribution of the mixing
159 amount and the rate of decay of scalar variance. A fixed value is used here
160 for simplicity, but this can be replaced to allow variations.

161 **3. Results**

162 *3.1. Simulated experiment*

163 The experiment [29] studied here is a methane-air jet (CH_4 33% v.v.) with
164 a velocity of 100 m/s and pipe diameter of 4.57 mm (jet $\text{Re} = 28,000$). The
165 coflow was air vitiated with H_2 (lean: $\Phi = 0.40$) and burned prior to being
166 released as coflow at 5.4 m/s and 1350 K. The typical behavior of this setup
167 is a lifted flame where the liftoff height is very sensitive to the inflow speeds
168 and temperature. This case is challenging for models because predicting the
169 liftoff behavior accurately requires suitable treatment of extinction/reignition
170 behavior.

171 The model was implemented into a parabolic code used successfully in
172 a previous study of the current vitiated flow [34]. In each simulation, there
173 were 80 cells in the radial direction, with the width of the domain increasing
174 as the entrained region grew. There was also variable spacing in the axial
175 direction, with $\Delta z/d = 1.5 \times 10^{-3}$ initially, linearly increasing to $\Delta z/d = 0.05$
176 at $z/d = 10$, then subsequently linearly increasing up to $\Delta z/d = 0.11$ in the
177 range $30 < z/d < 60$. On average, 400 particles were used in each cell, with
178 an ensemble of 10 simulations. Direct integration of the chemistry was used
179 in order to eliminate interpolation errors. The reduced chemical mechanism

180 comprises 48 species (28 in steady-state) and 300 reactions [7].

181 3.2. Mean statistics

182 The mean statistics were averaged over a spatial resolution of $\Delta z/d = 0.5$,
183 with no spatial averaging in the radial direction, then averaged over the
184 ensemble. The ensemble standard deviation is computed from the Favre
185 mean from each of the 10 simulations in the ensemble. The centerline mean
186 mixture fraction (Fig. 1) and temperature (Fig. 2) show good agreement
187 for most of the domain, generally reproducing the behavior near the outlet
188 and the axial stabilization point of the lifted flame. From the small ensemble
189 standard deviation in all the results, 400 particles/cell appears to be sufficient
190 to resolve the flow. The centerline rms mixture fraction (Fig. 3) tends to be
191 under-predicted downstream, which is likely due to excessive mixing in this
192 region, but the location and magnitude of the maximum is reproduced. The
193 temperature rms (Fig. 4) is well reproduced for $z/d < 70$, which accounts
194 for most of the important features of the flow. The temperature rms is
195 predicted significantly better than other models [29]. The species centerline
196 distributions are all generally well predicted, with the O_2 , OH and CO profiles
197 shown in Fig. 5. Further species are included in the Supplemental Material.

198 The radial profiles of mean mixture fraction (Fig. 6) and mean tempera-
199 ture (Fig. 7) generally agree with the experimental data. The radial locations
200 of the local maxima in the temperature around the base of the lifted flame
201 ($40 \leq z/d \leq 50$) are predicted well, as is the edge of the coflow. Like the cen-
202 terline results, the standard deviations tend to be modestly underpredicted.

203 Most results presented so far are similar to those obtained using the MC
204 model [34]. The exception is the centerline temperature rms, where the au-

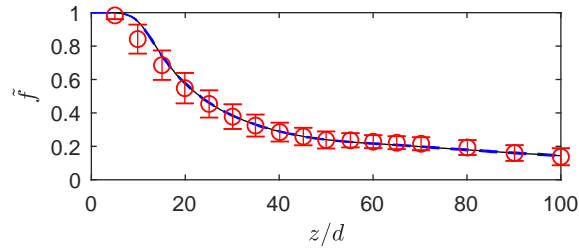


Figure 1: Centerline Favre-average mixture fraction. Hybrid model: ensemble mean, —; ensemble std either side of ensemble mean, - -. Experiment [29], \circ .

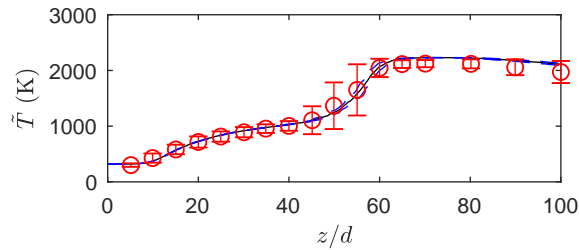


Figure 2: Centerline Favre-average temperature. As per Fig. 1.

205 thors have not found a RANS simulation that can correctly predict the loca-
 206 tions of both the rise at $z/d \simeq 40$ and the decrease at $z/d \simeq 60$. Of the LES
 207 simulations that report the temperature rms, some cannot simultaneously
 208 predict both these locations [35, 36]. Others that do predict the centerline
 209 temperature rms cannot predict a local maxima in the radial profile of mean

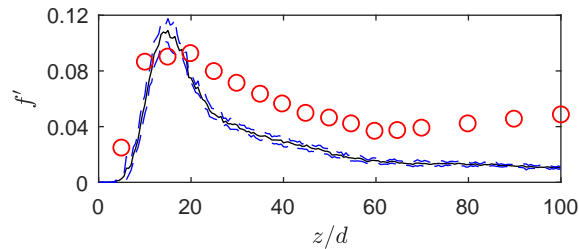


Figure 3: Centerline rms mixture fraction. As per Fig. 1.

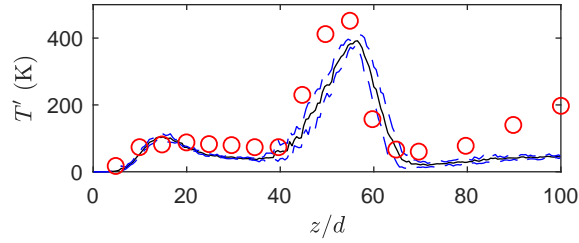


Figure 4: Centerline rms temperature. As per Fig. 1.

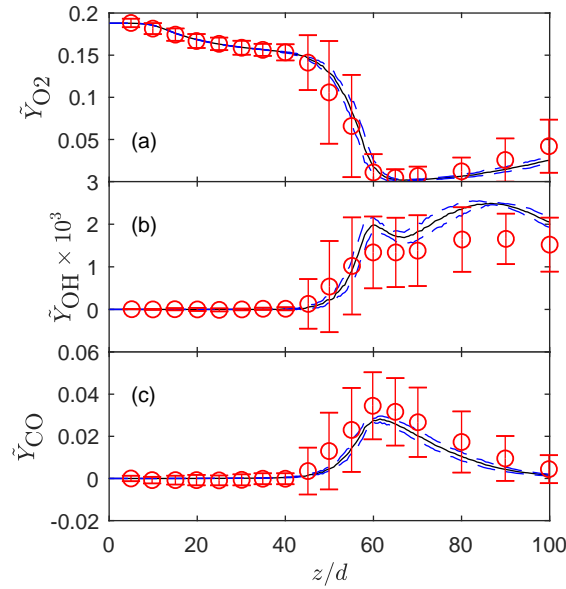


Figure 5: Centerline Favre-average mass fractions. (a) O₂; (b) OH; (c) CO. As per Fig. 1.

210 temperature at $z/d = 40$ [37, 38].

211 3.3. Conditional statistics

212 To properly understand the conditional statistics, the mixture fraction
 213 PDF is reported in Fig. 8. The general shape of the experiment is repro-
 214 duced; the δ -function at $f = 0$ shows that the coflow is resolved through-
 215 out the domain; while the maximum mixture fraction decays with distance

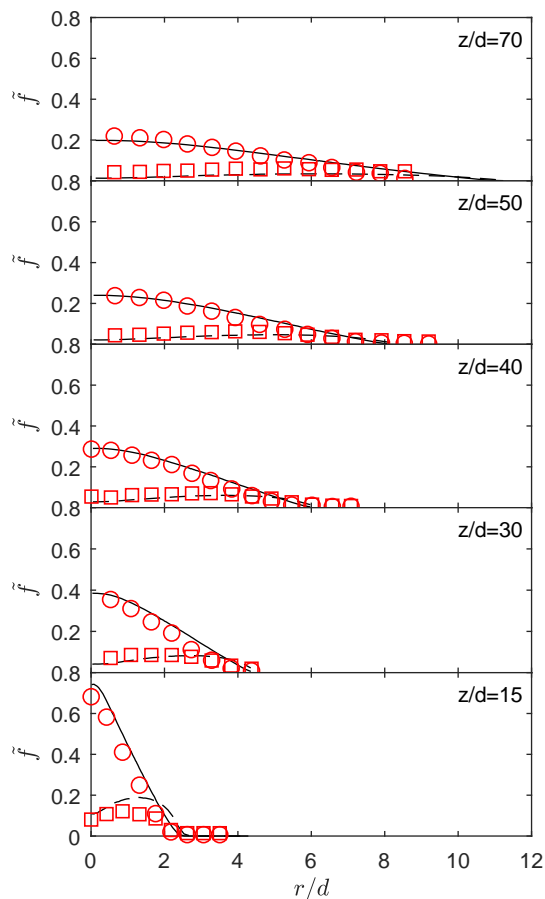


Figure 6: Radial mixture fraction at different axial locations. Hybrid model: mean, —; rms, --. Experiment [29]: mean, \circ ; rms, \square .

216 downstream somewhat faster than the experiment, which causes the slight
 217 underprediction of the standard deviation.

218 The scatter plots of temperature with respect to mixture fraction (Fig. 9)
 219 show that there is broad agreement with the experimental data. The results
 220 presented here are qualitatively similar to the corresponding MC results [34].
 221 The major difference is that by localizing the mixing, the particles tend to
 222 be richer for the same temperature, in closer agreement with experiment.

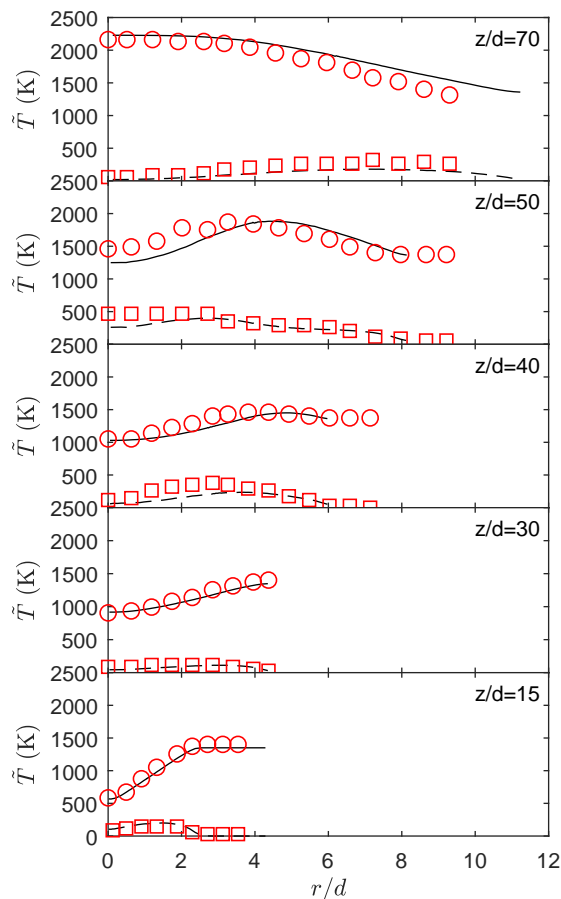


Figure 7: Radial temperature at different axial locations. As per Fig. 6.

223 Comparing to other computational results [29], for $z/d \leq 40$ there are
 224 frozen particles across most of the range of mixture fraction, in line with
 225 the experiments. At $z/d = 30$, no particles are close to equilibrium, un-
 226 like other studies. There is notable divergence between experimental data
 227 and all previous studies at $z/d = 40$. The current results and past MC re-
 228 sults [29, 34] appear similar at $z/d = 50$ and reproduce the band of particles
 229 at stoichiometric-to-rich mixture fractions which span the frozen and equi-

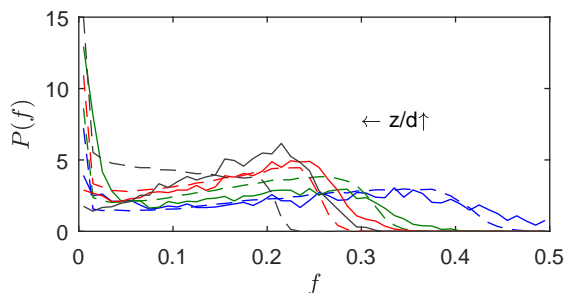


Figure 8: Mixture fraction PDFs. Hybrid model, - -; experiment [29], —. $z/d = 30$, —; 40, —; 50, —; 70, —.

230 librium limits. However, unlike the MC results [29, 34], local extinction is
 231 limited at $z/d = 70$, resulting in better agreement with the experimental
 232 data.

233 Conditional averaging of these results (Fig. 10) shows that the current
 234 approach predicts the near-frozen nature of the flow at $z/d = 30$, while
 235 repeating the MC model behaviour [29] of the conditional mean being the
 236 equilibrium temperature for a large portion of the lean part of the domain
 237 further downstream. The lean portion (the stoichiometric mixture fraction
 238 is 0.177 [29]) is predicted well by the current model, while other studies over-
 239 predict the temperature in this region [29]. Following this trend, the current
 240 results under-predict the conditional temperature for the rich region (partic-
 241 ularly at $z/d = 50$) in contrast to other studies [29]. The behavior of MMC
 242 in the rich region can be attributed to the lower centerline mixture fraction
 243 rms. Ironically, the latter creates a good prediction at $z/d = 70$, where
 244 the MMC results slightly over-predict the experiment for the entire range of
 245 mixture fractions. Conditional statistics for some species are included in the
 246 Supplemental Material and tend to mirror the predictions of temperature.

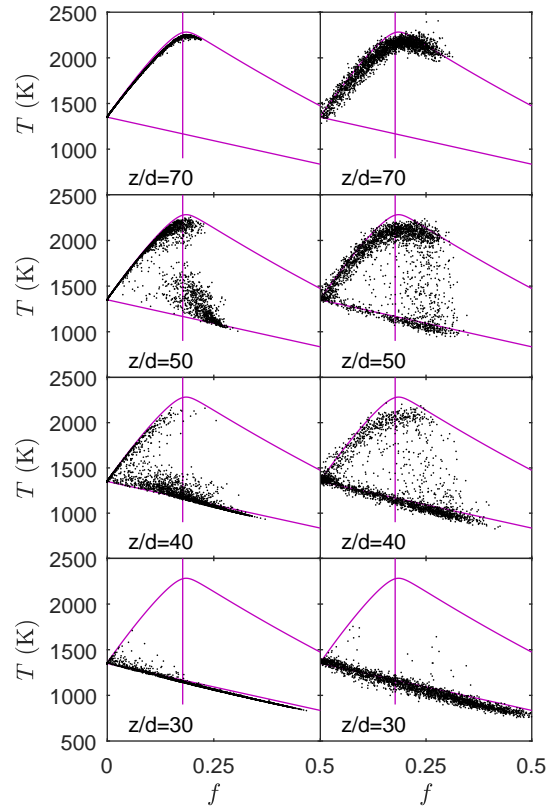


Figure 9: Scatter plots of temperature versus mixture fraction for the hybrid model (left) and experiment [29] (right). There are 2500 randomly-selected data points shown for each axial location. Equilibrium (upper) and frozen (lower) limits, and stoichiometric mixture fraction (vertical line): —.

247 3.4. Flame liftoff height

248 The flame liftoff height was calculated by averaging the axial locations
 249 where the mole fraction of C_2H_4 reached 100 ppm and C_2H_2 reached 2 ppm [29].
 250 For the base conditions, the liftoff height was found to be $H/D = 42$, some-
 251 what larger than the experimental value of 35 [29]. Similar to previous re-
 252 sults [29], there is little sensitivity to coflow velocity (Fig. 11), although the

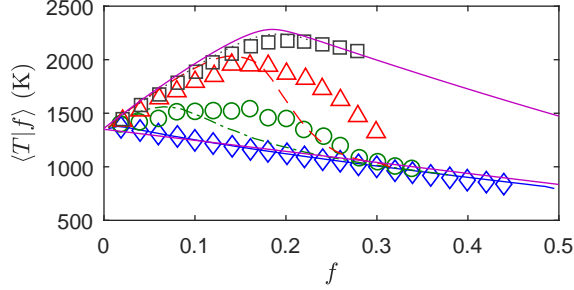


Figure 10: Temperature conditioned on mixture fraction. Hybrid model: $z/d = 30$, —; 40, - -; 50, - - -; 70, ···. Experiment [29]: $z/d = 30$, \diamond ; 40, \circ ; 50, \triangle ; 70, \square . Equilibrium (upper) and frozen (lower) limits: —.

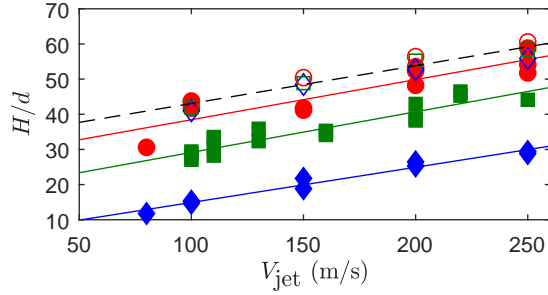


Figure 11: Lift-off height as function of jet velocity. Coflow velocity: 4.2 m/s, \diamond ; 5.3 m/s, \square ; 6.5 m/s, \circ . Hybrid model: open symbols with linear curve-fit of all results, - -. Experiment [29]: closed symbols with linear curve-fit of each coflow velocity, —.

253 current results predict a much larger lift-off height. The general trend of a
 254 monotonic decrease in lift-off height with increasing coflow temperature is
 255 reproduced (Fig. 12), with a lower sensitivity of lift-off height to coflow tem-
 256 perature, consistent with the MC model results using the same code [34].
 257 The insensitivity to coflow conditions could be caused by the mixing model
 258 and future improvements may contribute to a greater sensitivity to coflow
 259 conditions.

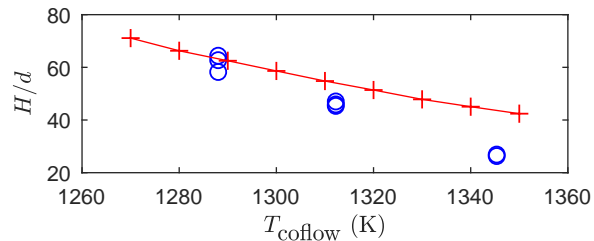


Figure 12: Liftoff height as function of coflow temperature. Hybrid model, +. Experiment [29], o.

260 4. Conclusions

261 A modified version of the hybrid binomial Langevin–Multiple Mapping
 262 Conditioning model has been proposed with the reference variable modeled
 263 by the mixture fraction from BLM. This approach promises to improve upon
 264 the applicability of the previous formulation [9, 10], while resulting in a
 265 simpler implementation. The development of a universal methodology that
 266 imposes a physical condition on the fraction of particles to be mixed remains
 267 desirable. However, it appears that the current augmented MC model, which
 268 imposes local mixing of particles in reference space, removes the tendency of
 269 the standard MC model to over-predict local extinction. The model was
 270 evaluated for a lifted jet flame [29], with the results generally comparing
 271 favorably with experimental data and previous modeling efforts.

272 Acknowledgments

273 The current work was, in part, performed at Imperial College while Dr
 274 Wandel was on sabbatical. The authors are grateful to Mr P. Simatos for
 275 technical support in conducting the simulations.

276 **References**

- 277 [1] G. Coppola, B. Coriton, A. Gomez, *Combust. Flame* 156 (2009) 1834–
278 1843.
- 279 [2] Y. Shoshin, J. Jarosinski, *Proc. Combust. Inst.* 32 (2009) 1043–1050.
- 280 [3] U. Do Lee, C.S. Yoo, J.H. Chen, J.H. Frank, *Proc. Combust. Inst.* 32
281 (2009) 1059–1066.
- 282 [4] S. Delhay, L.M.T. Somers, J.A. van Oijen, L.P.H. de Goey, *Proc. Com-
283 bust. Inst.* 32 (2009) 1051–1058.
- 284 [5] N. Peters, *Proc. Combust. Inst.* 32 (2009) 1–25.
- 285 [6] S.B. Pope, *Combust. Flame* 27 (1976), 299–312.
- 286 [7] R. Lindstedt, S. Louloudi, J. Driscoll, V. Sick, *Flow, Turb. Combust.* 72
287 (2004) 407–426.
- 288 [8] Z. Ren, S.B. Pope, *Combust. Flame* 136 (2004) 208–216.
- 289 [9] A.P. Wandel, R.P. Lindstedt, *Phys. Fluids* 21 (2009) 015103.
- 290 [10] A.P. Wandel, R.P. Lindstedt, *Proc. Combust. Inst.* 34 (2013) 1365–1372.
- 291 [11] L. Valiño, C. Dopazo, *Phys. Fluids A* 3 (12) (1991) 3034–3037.
- 292 [12] A.Y. Klimenko, S.B. Pope, *Phys. Fluids* 15 (7) (2003) 1907–1925.
- 293 [13] T. Hůlek, R.P. Lindstedt, *Combust. Sci. Tech.* 136 (1998) 303–331.
- 294 [14] S.B. Pope, *Flow, Turb. Combust.* 72 (2004) 219–243.

- 295 [15] A.Y. Klimenko, R.W. Bilger, *Prog. Energy Combust. Sci.* 25 (6) (1999)
296 595–687.
- 297 [16] M.J. Cleary, A. Kronenburg, *Proc. Combust. Inst.* 31 (2007) 1497–1505.
- 298 [17] M.J. Cleary, A. Kronenburg, *Combust. Flame* 151 (2007) 623–638.
- 299 [18] K. Vogiatzaki, A. Kronenburg, M.J. Cleary, J.H. Kent, *Proc. Combust.*
300 *Inst.* 32 (2009) 1679–1685.
- 301 [19] A.Y. Klimenko, in: *Clean Air*, Vol. 7, 2003, p. 14.4.
- 302 [20] A.P. Wandel, A.Y. Klimenko, *Phys. Fluids* 17 (12) (2005) 128105.
- 303 [21] C. Straub, S. De, A. Kronenburg, K. Vogiatzaki, *Combust. Theory Mod-*
304 *elling* 20 (5) (2016) 894–912.
- 305 [22] A. Varna, M.J. Cleary, E.R. Hawkes, *Combust. Flame* 181 (2017) 342–
306 353.
- 307 [23] A. Varna, M.J. Cleary, E.R. Hawkes, *Combust. Flame* 181 (2017) 354–
308 364.
- 309 [24] M.J. Cleary, A.Y. Klimenko, *Flow, Turb. Combust.* 82 (2009) 477–491.
- 310 [25] M.J. Cleary, A.Y. Klimenko, in: T. Echehki, E. Mastorakos (Eds.),
311 *Turbulent Combustion Modeling*, Springer, 2011, pp. 143–173.
- 312 [26] K. Ghai, S. De, K. Vogiatzaki, M.J. Cleary, in: S. De, A.K. Agarwal,
313 S. Chaudhuri, S. Sen (Eds.), *Modeling and Simulation of Turbulent*
314 *Combustion, Energy, Environment, and Sustainability*, Springer, Singa-
315 pore, 2018, pp. 447–474.

- 316 [27] B. Sundaram, A.Y. Klimenko, M.J. Cleary, Y. Ge, *Combust. Theory*
317 *Modelling* 20 (4) (2016) 735–764.
- 318 [28] S.Vo, O.T. Stein, A. Kronenburg, M.J. Cleary, *Combust. Flame* 179
319 (2017) 280–299.
- 320 [29] R. Cabra, J.-Y. Chen, R.W. Dibble, A.N. Karpetis, R.S. Barlow, *Com-*
321 *bust. Flame* 143 (2005) 491–506.
- 322 [30] A.P. Wandel, *Combust. Theory Modelling* 17 (4) (2013) 707–748.
- 323 [31] C. Dopazo, *Phys. Fluids* 22 (1979) 20.
- 324 [32] J. Janicka, W. Kolbe, W. Kollmann, *J. Non-Equilib. Thermodyn.* 4 (1)
325 (1979) 47–66.
- 326 [33] B. Sundaram, A.Y. Klimenko, *Proc. Combust. Inst.* 36 (2017) 1937–
327 1945.
- 328 [34] K. Gkagkas, R.P. Lindstedt, *Proc. Combust. Inst.* 31 (2007) 1559–1566.
- 329 [35] M. Ihme, Y.C. See, *Combust. Flame* 157 (2010) 1850–1862.
- 330 [36] O. Schulz, T. Jaravel, T. Poinso, B. Cuenot, N. Noiray, *Proc. Combust.*
331 *Inst.* 36 (2017) 1637–1644.
- 332 [37] P. Domingo, L. Vervisch, D. Veynante, *Combust. Flame* 152 (2008) 415–
333 432.
- 334 [38] N. Enjalbert, P. Domingo, L. Vervisch, *Combust. Flame* 159 (2012) 336–
335 352.

336 **Figure Captions**

337 Figure 1: Centerline Favre-average mixture fraction. Hybrid model: en-
338 semble mean, —; ensemble std either side of ensemble mean, - -. Experi-
339 ment [29], \circ .

340 Figure 2: Centerline Favre-average temperature. As per Fig. 1.

341 Figure 3: Centerline rms mixture fraction. As per Fig. 1.

342 Figure 4: Centerline rms temperature. As per Fig. 1.

343 Figure 5: Centerline Favre-average mass fractions. (a) O_2 ; (b) OH ;
344 (c) CO . As per Fig. 1.

345 Figure 6: Radial mixture fraction at different axial locations. Hybrid
346 model: mean, —; rms, - -. Experiment [29]: mean, \circ ; rms, \square .

347 Figure 7: Radial temperature at different axial locations. As per Fig. 6.

348 Figure 8: Mixture fraction PDFs. Hybrid model, - -; experiment [29], —.
349 $z/d = 30$, —; 40 , —; 50 , —; 70 , —.

350 Figure 9: Scatter plots of temperature versus mixture fraction for the
351 hybrid model (left) and experiment [29] (right). There are 2500 randomly-
352 selected data points shown for each axial location. Equilibrium (upper) and
353 frozen (lower) limits, and stoichiometric mixture fraction (vertical line): —.

354 Figure 10: Temperature conditioned on mixture fraction. Hybrid model:
355 $z/d = 30$, —; 40 , - ·; 50 , - -; 70 , ···. Experiment [29]: $z/d = 30$, \diamond ; 40 , \circ ;
356 50 , \triangle ; 70 , \square . Equilibrium (upper) and frozen (lower) limits: —.

357 Figure 11: Liftoff height as function of jet velocity. Coflow velocity:
358 4.2 m/s, \diamond ; 5.3 m/s, \square ; 6.5 m/s, \circ . Hybrid model: open symbols with linear
359 curve-fit of all results, - -. Experiment [29]: closed symbols with linear
360 curve-fit of each coflow velocity, —.

361 Figure 12: Liftoff height as function of coflow temperature. Hybrid
362 model, +. Experiment [29], o.

363 **List of Supplemental Material**

364 Figure S1: Centerline Favre-average CO₂ mass fraction. Hybrid model:
365 ensemble mean, —; ensemble std either side of ensemble mean, - -. Experi-
366 ment [29], ○.

367 Figure S2: Centerline Favre-average CH₄ mass fraction. Hybrid model:
368 ensemble mean, —; ensemble std either side of ensemble mean, - -. Experi-
369 ment [29], ○.

370 Figure S3: Centerline Favre-average H₂ mass fraction. Hybrid model:
371 ensemble mean, —; ensemble std either side of ensemble mean, - -. Experi-
372 ment [29], ○.

373 Figure S4: Centerline Favre-average H₂O mass fraction. Hybrid model:
374 ensemble mean, —; ensemble std either side of ensemble mean, - -. Experi-
375 ment [29], ○.

376 Figure S5: Scatter plots of temperature versus mixture fraction (2500
377 randomly-selected data points shown for each axial location). Equilibrium
378 (upper) and frozen (lower) limits, and stoichiometric mixture fraction (ver-
379 tical line): —.

380 Figure S6: Temperature conditioned on mixture fraction. Hybrid model:
381 $z/d = 30$, —; 40 , - ·; 50 , - -; 70 , ···. Experiment [29]: $z/d = 30$, ◇; 40 , ○;
382 50 , △; 70 , □. Equilibrium (upper) and frozen (lower) limits: —.

383 Figure S7: Rms of conditional temperature. Hybrid model: $z/d = 30$, —;
384 40 , - ·; 50 , - -; 70 , ···. Experiment [29]: $z/d = 30$, ◇; 40 , ○; 50 , △; 70 , □.

385 Figure S8: Scatter plots of O₂ mass fraction versus mixture fraction
386 for the hybrid model (left) and experiment [29] (right). There are 2500
387 randomly-selected data points shown for each axial location. Equilibrium

388 (lower) and frozen (upper) limits, and stoichiometric mixture fraction (ver-
389 tical line): —.

390 Figure S9: O₂ mass fraction conditioned on mixture fraction. Hybrid
391 model: $z/d = 30$, —; 40, — ·; 50, — —; 70, ···. Experiment [29]: $z/d = 30$, ◇;
392 40, ○; 50, △; 70, □. Equilibrium (lower) and frozen (upper) limits: —.

393 Figure S10: Rms of conditional O₂ mass fraction. Hybrid model: $z/d =$
394 30, —; 40, — ·; 50, — —; 70, ···. Experiment [29]: $z/d = 30$, ◇; 40, ○; 50, △;
395 70, □.

396 Figure S11: Scatter plots of OH mass fraction versus mixture fraction
397 for the hybrid model (left) and experiment [29] (right). There are 2500
398 randomly-selected data points shown for each axial location. Equilibrium,
399 and stoichiometric mixture fraction (vertical line): —.

400 Figure S12: OH mass fraction conditioned on mixture fraction. Hybrid
401 model: $z/d = 30$, —; 40, — ·; 50, — —; 70, ···. Experiment [29]: $z/d = 30$, ◇;
402 40, ○; 50, △; 70, □. Equilibrium: —.

403 Figure S13: Rms of conditional OH mass fraction. Hybrid model: $z/d =$
404 30, —; 40, — ·; 50, — —; 70, ···. Experiment [29]: $z/d = 30$, ◇; 40, ○; 50, △;
405 70, □.